Adaptive Current Control Strategy for Harmonic Compensation in Single-Phase Solar Inverters

Lucas S. Xavier[a,c], Allan F. Cupertino[b], José T. de Resende[a], Victor F. Mendes[c], Heverton A. Pereira[a,*]

[a] *Electric Engineering Department, Federal University of Viçosa, 36570–900, Viçosa, Brazil*
[b] *Department of Materials Engineering, Federal Center for Technological Education of Minas Gerais, Av. Amazonas 5253, 30421-169, Belo Horizonte - MG, Brazil*
[c] *Department of Electrical Engineering, Federal University of Minas Gerais, Av. Pres. Antônio Carlos, 6627, Belo Horizonte - MG, Brazil*

Abstract

Nowadays, the power systems are submitted to current and voltage harmonics due to the increased presence of nonlinear loads and the wide use of power inverters to interface solar and wind power plants. Nevertheless, these inverters can also be used to compensate the current harmonics. Traditional harmonic detection methods extracts all harmonic current information and the control tuning tends to be complex and less flexible. Therefore, this work proposes an adaptive current harmonic control strategy applied in multifunctional single-phase solar inverters. The strategy is based on a novel detection method of the harmonic load current. The harmonic current detection method is frequency adaptive and designed to extract the load harmonic current with higher amplitude. The detected harmonic is compensated using an adaptive proportional resonant (PR) controller, reducing the grid current total harmonic distortion (THD). The detection method consists of two-cascaded phase-locked loop based on second order generalized integrator (SOGI-PLL) which uses the detected frequency to automatically tune the PR. The proposed method is explored in terms of nondetection zone, the impact of the SOGI-PLL parameters and the control stability analysis. Simulation and experimental results show the performance of

*Corresponding author
Email address: heverton.pereira@ufv.br (Heverton A. Pereira)

the proposed control strategy, reducing significantly the grid current distortion.

Keywords: Adaptive control, harmonic compensation, harmonic current detection method, SOGI-PLL, grid-connected photovoltaic system, proportional resonant controller

2010 MSC: 00-01, 99-00

1. Introduction

For the first time in four decades, the global carbon emissions related to energy consumption remained stable in 2014, while the global economy grew [1]. The high penetration level of renewable energy sources in the global electrical system is the reason associated with this stabilization [1]. However, some concerns are emerging due to the growth of renewable energy sources integration, especially wind and photovoltaic (PV) sources, into the electric power system such as: quality of the energy injected into the grid [2, 3], security and support under grid faults [4, 5, 6], voltage regulation at the point of common coupling (PCC) during grid voltage sags [7], harmonic current compensation [8, 9, 10] and reactive power compensation [11].

The expansion of the electrical devices with nonlinear characteristic in the current and voltage relation have caused, for several years, concerns about the proliferation of harmonics in the power system [12, 13, 14]. Details about the nonlinear load behaviour is addressed in [15]. Devices such as power electronic converters, fluorescent lamps, electronic ballasts, thyristors, computers can lead to higher harmonic current levels which are responsible for efficiency reduction in the power grid, besides interacting with resonances present in the system [13, 14, 16]. Due to this fact, the IEEE and IEC harmonic standards contains recommendations for harmonic limitation at the point of common couple [16, 17].

The use of power converters to interface renewable sources with the power system is regulated by grid codes in order to ensure the grid power quality. However, these devices can also improve the power quality of an installation.

Several works show that PV inverters have been employed to compensate the harmonic current generated by nonlinear loads connected at the PCC. However, this ancillary service is limited by the converter rated current [8, 9, 10].

The main objective of the PV systems is to supply active power to the load/grid, but as generally the converter is operating below its rated current, the current margin can be used for the harmonic compensation. During the night, for example, all the converter current capability can be used for harmonic compensation.

Many issues need to be defined in order to use photovoltaic inverter to compensate harmonic currents. The first one is the harmonic current detection method. Different strategies have been proposed in the literature. References [8, 9, 10, 18] apply the conservative power theory for current decomposition in three orthogonal components, the active, reactive and residual current component. In [19, 20, 21] it is used the instantaneous power theory to separate the current in average and oscillating components. Reference [22] uses the instantaneous symmetrical components theory for extracting the reference currents. It should be emphasized that the detected harmonic current by the traditional methods contains all harmonic orders, and it increases the controller tuning complexity. Therefore, the additional computational processing is necessary to identify individual harmonic currents [23].

In single-phase applications with harmonic compensation, many works use proportional-resonant (PR) controllers, due to the presence of many frequencies in inverter current reference [24, 25]. In these conditions, the conventional proportional-integral (PI) controller has steady state error due to its limited current tracking capability [24]. On the other hand, a PR controller must be tuned for each harmonic frequency in order to compensate the harmonic currents, increasing the control algorithm complexity [25].

This work proposes a harmonic detector algorithm which detects only the harmonic content with higher amplitude in the load current, and uses this information in the harmonic compensation process. If the harmonic current component with higher amplitude is eliminated, it is possible to reduce the grid

current THD with low control algorithm complexity. This method consists of two-cascaded synchronous reference frame phase-locked loop (SRF-PLL) based on second order generalized integrator (SOGI-PLL) proposed in [26]. The harmonic controller consists of a proportional multi-resonant (PMR) controller whose resonance is frequency adaptive. The utilization of adaptive resonant controllers is addressed in [27, 28] with focus to minimize the controller degradation associated with grid frequency deviation.

In view of the above discussions, the contributions of this paper are: a novel harmonic current detection method applied in single-phase PV inverters is proposed; analysis of a nondetection zone when harmonic components with similar amplitude are present in the load current; stability analysis of the adaptive resonant controller during variation in its resonant frequency.

This work is organized into the following sections. Section 2 introduces a discussion about the novel harmonic current detection method and its application in adaptive current control strategy. Section 3 presents the dynamic behaviour of the proposed harmonic detector as well as the stability of the adaptive control. Section 4 presents the simulation and experimental results to validate the proposed control strategy. Finally, conclusions are stated in Section 5.

2. Adaptive Current Harmonic Control Strategy

2.1. Control Strategy

Generally, in single-phase PV system, the dc/dc stage with a boost converter is used to keep the desired dc-link voltage constant [2], as shown in Fig. 1a. The boost control strategy is shown in Fig. 1b, which consists of an outer loop, responsible for controlling the dc-bus voltage of the solar array v_{pv}, and an inner loop, responsible for controlling the current of the boost inductor I_{ind}. The voltage reference for the dc/dc stage loop is calculated by a maximum power point tracking (MPPT) algorithm, which maintains the solar array delivering the maximum power to the system at various levels of solar irradiance

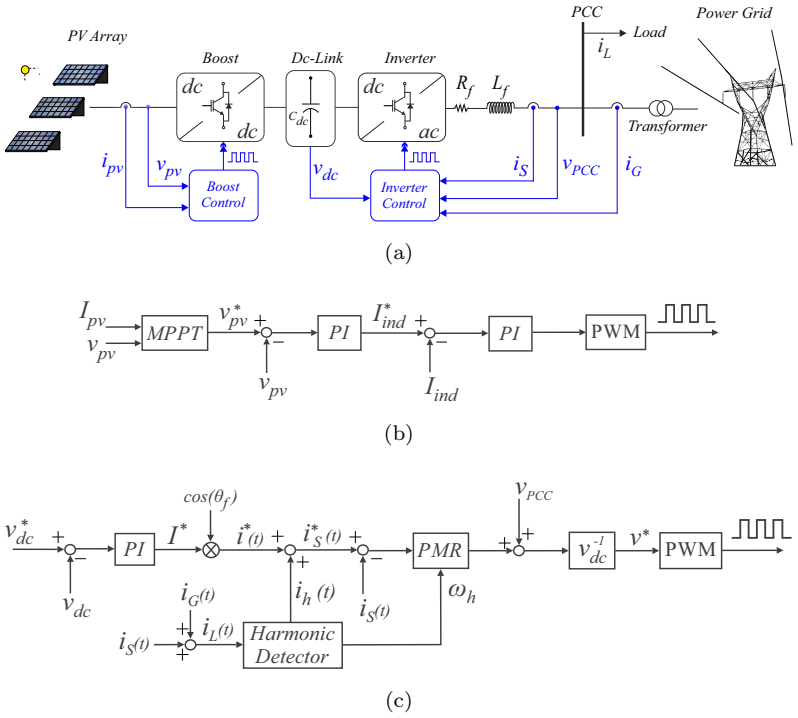

Figure 1: (a) Single-phase grid-connected photovoltaic system, (b) Boost control loop, (c) Inverter control loop.

and temperature [29]. The electrical model of the solar panel is based on the mathematical model proposed in [30].

The inverter control strategy is shown in Fig. 1c. A PI compensator is used in the dc-link voltage control. This compensator calculates the active current amplitude I^* which will be injected into the power system. This signal is synchronized with PCC voltage and added to harmonic component detected by the proposed strategy. Finally, the controller calculates the converter modulation index v^*.

The control system is based on PMR controller composed of: a proportional controller, a resonant tuned to fundamental frequency and another resonant controller dynamically tuned at harmonic frequency provided by the proposed

harmonic detection method. The PMR transfer function is given by:

$$G_c(s) = K_p^r + \overbrace{K_{i_f}\frac{s}{s^2+\omega_f^2}}^{R_f(s)} + \overbrace{K_{i_h}\frac{s}{s^2+\omega_h^2}}^{R_h(s)}, \quad (1)$$

where K_p^r is the proportional gain. K_{if} and K_{ih} are the integral gains tuned at the fundamental frequency and harmonic order h, respectively, ω_f is the fundamental frequency and ω_h is the harmonic frequency provided by proposed harmonic detection method.

Using traditional harmonic detection methods, one resonant controller is necessary for each harmonic order. Aiming to reduce the number of resonant controllers, the proposed harmonic current detection method is able to detect only the harmonic component with higher amplitude. Thereby, only two resonant controllers are required: one of them for fundamental component and another with frequency adaptive characteristic for harmonic compensation.

The PMR controller has high gains at its resonant frequencies. Thereby, the terms R_f and R_h are responsible for tracking the current component at fundamental frequency ω_f and at harmonic frequency ω_h, respectively.

The discretization method used in $R_f(s)$ and $R_h(s)$ is the Tustin with pre-warping. This technique avoids a displacement of the poles [31]. The z-domain transfer function of the $R_f(s)$ and $R_h(s)$ is given by:

$$R_x(z) = \frac{sin(\omega_x T_s)}{2\omega_x}\frac{1-z^{-2}}{1-2z^{-1}cos(\omega_x T_s)+z^{-2}}, \quad (2)$$

where ω_x is the resonant frequency (ω_f or ω_h) and T_s is the sampling period.

2.2. Adaptive Harmonic Current Detection Method

The proposed harmonic current detection method is based on two cascaded SOGI-PLL, as shown in Fig. 2. The resonant frequency of the SOGI-based adaptive filter (SOGI-based AF) is provided by the SRF-PLL frequency feedback [2]. Furthermore, the harmonic current detection structure consists of two stages.

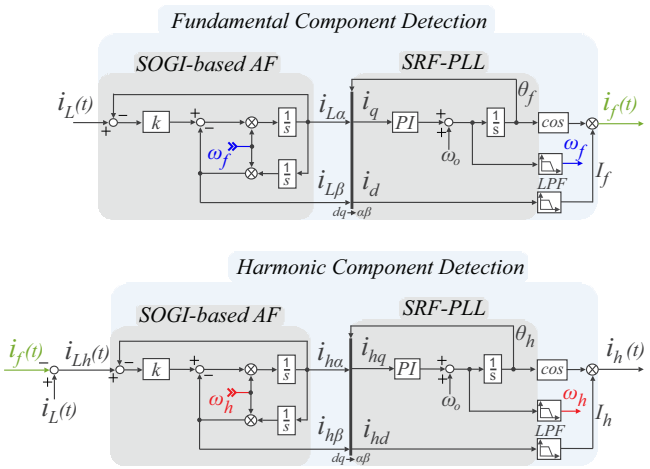

Figure 2: Current harmonic detection method based on two cascaded SOGI-PLL.

The first stage is responsible for detecting the parameters of the load current fundamental component such as its frequency ($\omega_f = 2\pi 60\ rad/s$) and amplitude.

In the SRF-PLL, the dq reference frame angular position is adjusted forcing i_q to zero [32]. Therefore, the amplitude of the current fundamental component I_f is equal to i_d filtered by a low-pass filter (LPF). Therefore, the fundamental current component $i_f(t)$ is detected as:

$$i_f(t) = I_f cos(\theta_f), \tag{3}$$

where θ_f is the fundamental component phase angle detected by the SRF-PLL. The total harmonic content $i_{Lh}(t)$ is determined by the difference between the load current $i_L(t)$ and $i_f(t)$.

The second stage is similar to the previous one. However, it is responsible for detecting the harmonic current component with higher amplitude. Its harmonic frequency ω_h and amplitude I_h are detected by the second SOGI-PLL. The harmonic component $i_h(t)$ is determined as:

$$i_h(t) = I_h cos(\theta_h), \tag{4}$$

where θ_h is the harmonic component phase angle of the load current with higher

amplitude. Furthermore, the second stage is also responsible for the adaptive characteristic of the proposed current control, i.e., the frequency is used to adjust the PMR controller.

In the next section, a detailed analysis is performed in order to stress the proposed methodology. Among the analysis, it is highlighted the SOGI-PLL tuning process, which should to ensure an admissible settling time with a flexible bandwidth to track the harmonic current component. Other important point is the effect of the low- pass filters (LPFs) cut-off frequency, which needs to avoid unwanted oscillations in the detected amplitude and frequency.

3. Harmonic Detector and Controller Stability Analysis

3.1. SOGI Gain Effect on the Harmonic Detection

For the proposed analysis, a load harmonic current $i_{Lh}(t)$ with harmonic frequency ω_h and amplitude I_h is considered, as given by:

$$i_{Lh}(t) = I_h cos(\omega_h t). \tag{5}$$

In this analysis, the SRF-PLL feedback frequency is assumed to ideally track down the frequency, i.e., the detected frequency is ω_h.The SOGI-based AF transfer functions are expressed as:

$$H_\alpha(s) = \frac{i_{Lh\alpha}(s)}{i_{Lh}(s)} = \frac{k\omega_h s}{s^2 + k\omega_h s + \omega_h^2}, \tag{6}$$

$$H_\beta(s) = \frac{i_{Lh\beta}(s)}{i_{Lh}(s)} = \frac{k\omega_h}{s^2 + k\omega_h s + \omega_h^2}. \tag{7}$$

These transfer functions show that the bandwidth of the SOGI-based AF only depends on the gain k. It can be observed that $i_{Lh\alpha}$ and $i_{Lh\beta}$ are two orthogonal currents and the Bode diagram of (6) and (7) are illustrated in Fig. 3a and Fig. 3b for several values of SOGI gain (k), respectively. It is seen that the signal attenuation increases with k, but with different shapes for $H_\alpha(s)$

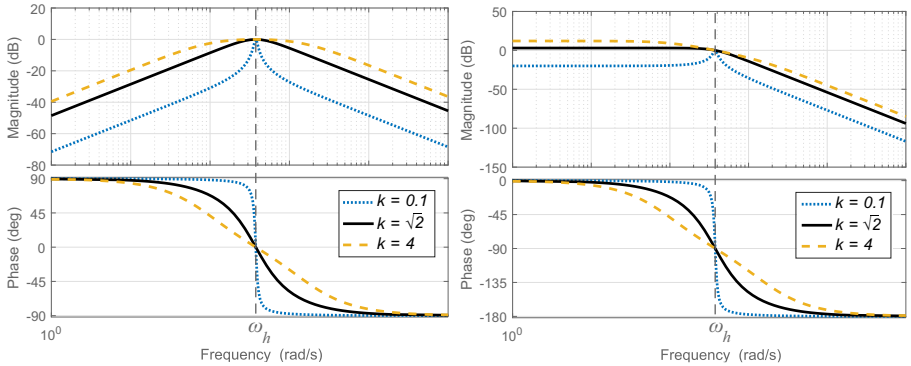

Figure 3: Bode diagrams of SOGI for several values of gain (k), (a) $H_\alpha(s)$ bode diagram and (b) $H_\beta(s)$ bode diagram.

and $H_\beta(s)$. This fact can influence in the harmonic signal detection and it is discussed in the following sections.

Applying Laplace transform in (5), replacing it in (6) and (7) and applying inverse Laplace transform, the time responses of the $i_{Lh\alpha}$ and $i_{Lh\beta}$ are:

$$i_{Lh\alpha}(t) = I_h cos(\omega_h t) - I_h e^{(-\frac{\omega_h k t}{2})} \left[cosh(A\omega_h t) - \frac{k sin(A\omega_h t)}{2A} \right], \tag{8}$$

$$i_{Lh\beta}(t) = I_h sin(\omega_h t) + \frac{I_h e^{(-\frac{\omega_h k t}{2})} sin(A\omega_h t)}{A}, \tag{9}$$

where $A = \sqrt{1 - \frac{k^2}{4}}$.

When $k = \sqrt{2}$, an optimal relationship between settling time and overshoot is achieved presenting a critically damped response. To verify the influence of the SOGI gain in frequency and amplitude detection, initially a 3rd harmonic order of amplitude 1 A is considered in the simulation. At 0.4 seconds, a 5th harmonic order component with amplitude equal to 3 A is added on the harmonic detector input. Fig. 4a and Fig. 4b show the frequency and amplitude detection response of the 5th harmonic component for several values of k, respectively.

It can be observed that for $k = 0.1$, the harmonic detector is not able to

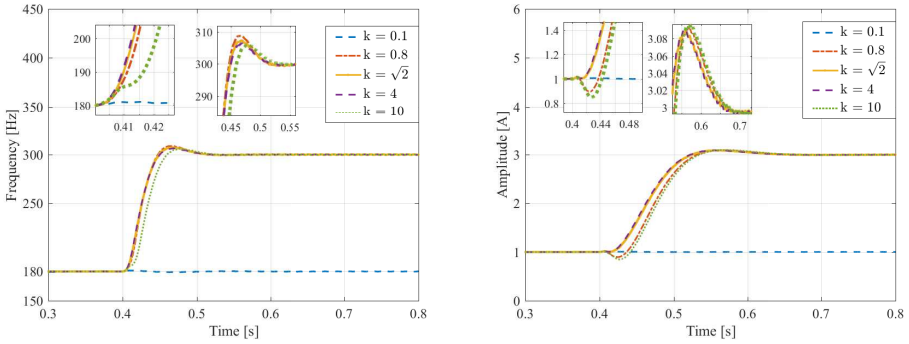

(a) (b)

Figure 4: Detected frequency and amplitude for several values of SOGI gain (k), (a) Detected frequency and (b) Detected amplitude.

detect the harmonic with higher amplitude due to the narrow bandwidth of the SOGI-based AF. On the other hand, a wide bandwidth can allow considerable overshooting in the SOGI outputs and it can affect the response time. $k = \sqrt{2}$ is used in following analysis and in the case study.

3.2. Frequency Filtering Effect on the Harmonic Detection

In the proposed harmonic detector method, the LPF has an important influence in the output characteristic, mainly when the harmonic detector input $i_{Lh}(t)$ has two or more harmonic components. Therefore, unwanted oscillations must be avoided in the amplitude and frequency detection process. In this work, the second order Butterworth low pass filters with cut-off frequencies f_{cf} (for frequency filtering) and f_{ca} (for amplitude filtering) are used.

Fig. 5a and Fig. 5b shows the influence of three f_{cf} and f_{ca} values (5 Hz, 10 Hz and 30 Hz) on frequency and amplitude detection of the 5th harmonic at 0.4 seconds, respectively. In steady state conditions, the frequency ripple is 1% for $f_{cf} = 30\ Hz$, as depicted in Fig. 5a, whereas the amplitude ripple for $f_{ca} = 30\ Hz$ is 4%, as shown in Fig. 5b. For $f_{cf} = 30\ Hz$, besides the direct component, there is an oscillation of 2nd harmonic in the detected frequency I_5, as shown in Fig. 5c. Therefore, unwanted 3rd and 7th harmonic components in

185 $i_{Lh}(t)$ arises in $i_h(t)$ by the product between the 2nd harmonic oscillation and the detected phase angle of the 5th harmonic content, which can be observed in (4) and Fig. 5d. In order to reduce the unwanted frequencies in the detected predominant harmonic and a fast detection response, for this work $f_{ca} = 5\ Hz$ and $f_{cf} = 10\ Hz$ are chosen.

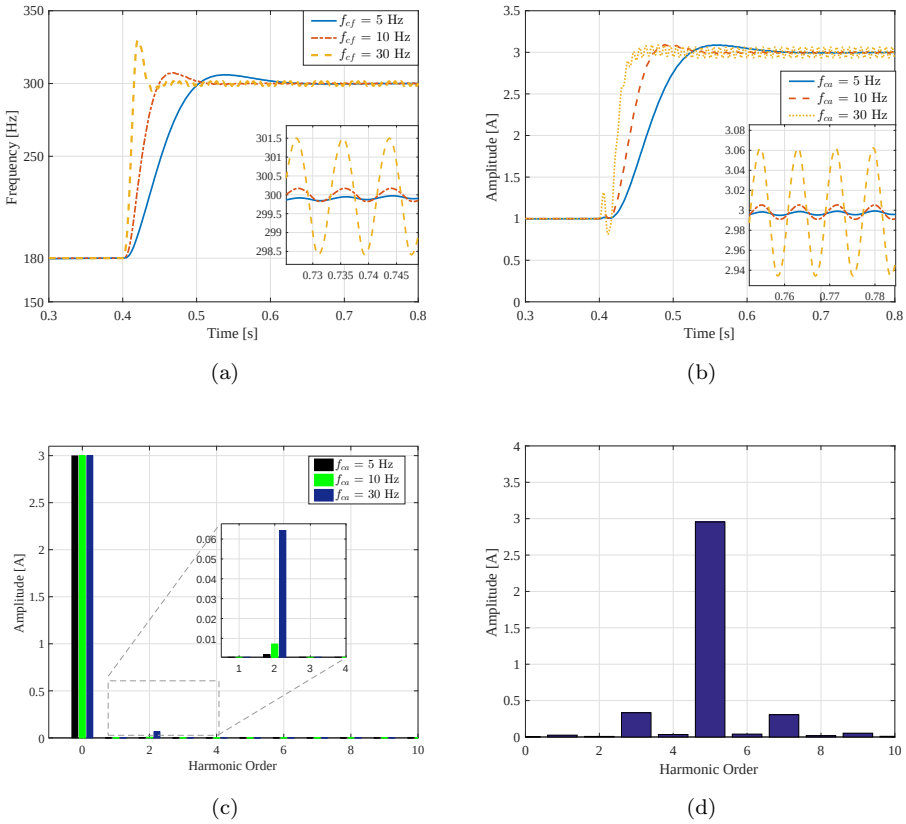

Figure 5: Detected frequency and amplitude for three different values for both cut-off frequencies (f_{cf} and f_{ca}) of the LPFs, considering $k = \sqrt{2}$, (a) Detected frequency for three f_{cf} values, (b) Detected amplitude for three f_{ca}, keeping $f_{cf} = 10\ Hz$, (c) Detected amplitude spectrum for three f_{ca} values, keeping $f_{cf} = 10\ Hz$ and (d)Detected $i_h(t)$ current spectrum, parameters: $f_{ca} = 30\ Hz$, $f_{cf} = 10\ Hz$ and $k = \sqrt{2}$.

3.3. SRF-PLL Natural Frequency Impact on the Harmonic Detection

The closed-loop transfer function of a SRF-PLL is given by [32]:

$$G_{PLL}(s) = \frac{\theta_h(s)}{\theta_{in}(s)} = \frac{k_p s + k_i}{s^2 + k_p s + k_i}, \tag{10}$$

where θ_h and θ_{in} are the output and input phase angle, respectively. k_p and k_i are the PI controller gains. The expression shown in (10) is a standard second-order transfer function. It is defined $k_p = 2\zeta\omega_n$ and $k_i = \omega_n^2$, where ζ is the damping factor and $\omega_n = 2\pi f_n$ is the SRF-PLL natural frequency.

In order to obtain an acceptable dynamic performance of the phase angle detection process, $\zeta = \frac{1}{\sqrt{2}}$ is recommended in the literature and ω_n is adjusted in accordance with the desired controller bandwidth. [2, 32].

The frequency and amplitude detection of the 5th harmonic component for some ω_n values are shown in Fig. 6a and Fig. 6b, respectively. It can be observed that for $f_n = 10\ Hz$, the amplitude and frequency of the 5th harmonic has not been detected. For $f_n = 100\ Hz$, an offset is observed in the detected amplitude due to SRF-PLL wide bandwidth. This wide bandwidth generates unwanted oscillations at the detected phase angle, and thus the dq reference frame angular position is affected. The acceptable relationship between settling time, unwanted oscillations suppressions and lower steady-state error is found for $f_n = 50\ Hz$.

3.4. Nondetection Zone of the Proposed Harmonic Detector

The main goal of the proposed harmonic detector is to track the predominant harmonic in the current signal. However, depending of the amplitude of the harmonic components, the detector cannot follow the harmonic with highest amplitude. In fact, there is a nondetection zone which can be explained by two factors. The first one is the SOGI bandwidth limitation. The second one is the capability of SRF-PLL follows the predominant harmonic component. The analysis for both phenomena are presented in this section.

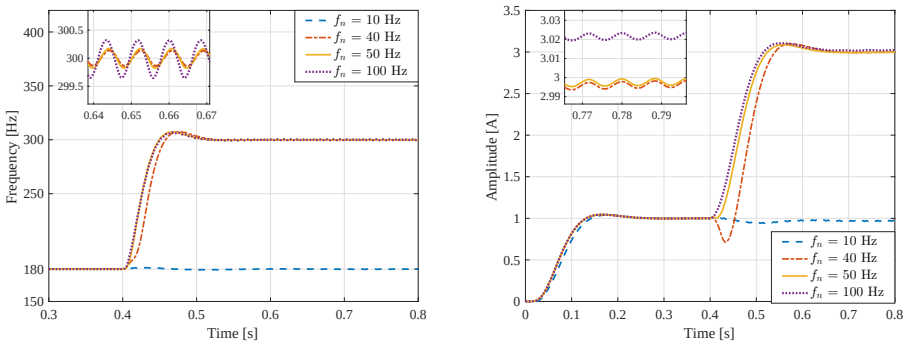

(a) (b)

Figure 6: Detected frequency and amplitude for some values of SRF-PLL natural frequency f_n. Parameters: $k = \sqrt{2}$, $f_{ca} = 5\ Hz$ and $f_{cf} = 10\ Hz$, (a) Detected frequency and (b) Detected amplitude.

3.4.1. Effect of SOGI bandwidth limitation

To evaluate the nondetection zone in terms of SOGI bandwidth limitation, a harmonic current composed of a 3rd and 5th harmonic components is applied in the harmonic detector input. Thereby, $i_{Lh}(t)$ is given by:

$$i_{Lh}(t) = I_3 cos(\omega_3 t) + I_5 cos(\omega_5 t), \tag{11}$$

where $\omega_3 = 2\pi 180\ rad/s$ and $\omega_5 = 2\pi 300\ rad/s$. I_3 and I_5 are the amplitudes of 3rd and 5th harmonic current, respectively.

The SRF-PLL feedback frequency is considered as ω_3 and $k = \sqrt{2}$. The magnitude Bode diagrams of SOGI structure are illustrated in Fig. 7a and Fig. 7b. When the amplitude of 5th harmonic current component becomes higher than the 3rd harmonic component ($I_5 > I_3$), the 5th harmonic content is detected as predominant harmonic if:

$$\overbrace{I_5 \cdot 0.798 > I_3}^{R_1} \, and \, \overbrace{I_5 \cdot 0.482 > I_3}^{R_2}, \tag{12}$$

where 0.798 and 0.482 are the magnitude gains at 300 Hz , as shown in Fig. 7a. and Fig. 7b, respectively. Once the magnitude gain at 180 Hz is unitary, if

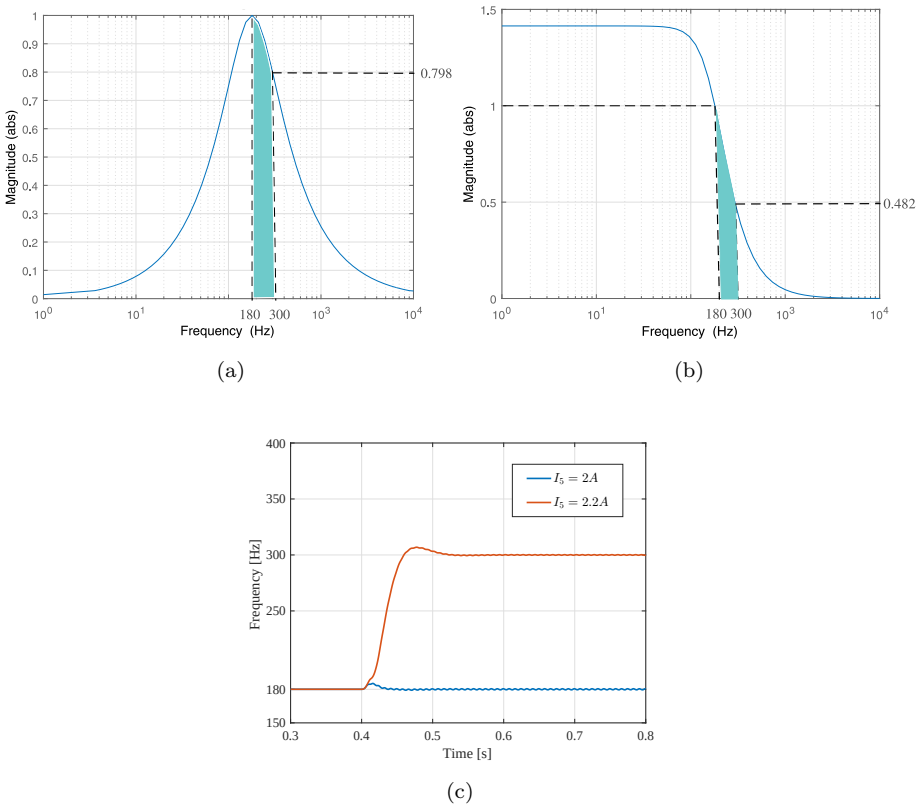

Figure 7: Magnitude bode diagrams of the SOGI for nondetection zone analysis and 5th harmonic component detection response, (a) H_α bode diagram, (b) H_β bode diagram and (c) 5th harmonic component detection response for two different value of I_5 at 0.4 seconds.

I_5 does not satisfy R_2 in (12), the 5th harmonic content is not detected.

In order to check (12) simulations are used. In 0.4 seconds, two different amplitude values of a 5th harmonic component (2 A and 2.2 A) are applied in (4), and the amplitude of the 3rd harmonic current signal is constant (1 A). Considering that the SRF-PLL natural frequency is 50 Hz, and $I_5 = 2$ A, the expression R_2 is not true. Therefore, the 5th harmonic component of the current is not detected, as shown in Fig. 7c. For $I_5 = 2.2$ A, the expression R_2 are true and the 5th harmonic content is detected, as shown in Fig. 7c.

3.4.2. SRF-PLL detection threshold

In fact, if the input signal of SRF-PLL is composed of two harmonics with similar amplitudes, the SRF-PLL can estimate the frequency incorrectly. In this condition, this work defines the PLL *detection threshold*, which consists in the minimum amplitude difference between two harmonic components which implies in the correct frequency detection. In order to understand the SRF-PLL detection threshold, firstly it is necessary to understand its dynamic behaviour during frequency changes (single harmonic approach).

The SRF-PLL is a nonlinear system. The transfer function presented in section 3.3 considers a locked state. However, for large frequency variation (change of harmonic content), this approach is not valid [33]. The study of PLLs modelling in unlocked state is related in some texts in literature [33, 34]. Using a similar methodology of [33], the SRF-PLL dynamics can be modelled by the following nonlinear differential equation:

$$\ddot{\theta}_e + \dot{\theta}_e k_p sin\theta_e + k_p cos\theta_e + k_i sin\theta_e = \ddot{\theta}_{in}, \tag{13}$$

where $\theta_e = \theta_h - \theta_{in}$ is the phase error.

The solution of this differential equation is not a trivial task [33]. Specialized texts evaluate the performance during unlock state using some key parameters obtained from some approximations and simulations analysis [33, 34, 2].

For two or more harmonic components, the determination of these parameters is more complex. Some texts in literature approaches this problem considering the main component much larger than other harmonics. In this case, these harmonic components can be modelled as a noise signal [34]. However, this approach is not valid for the proposed harmonic detector. Numerical solutions can be used in order to solve this problem, for specific values of ξ and ω_n. Thus, it is possible to estimate the SRF-PLL detection threshold.

To illustrate this process, initially, it is used a 1 pu of 3rd harmonic signal in the SRF-PLL input. When it reaches the steady-state, a 5th harmonic component is added in the SRF-PLL input signal. The amplitude value of 5th

harmonic component is slowly increased, in order to determine the SRF-PLL detection threshold.

The study case results are presented in Fig. 8. It can be observed that the detection threshold reduces significantly for large ξ and ω_n. However, large ξ results in poor dynamic behaviour as mentioned in [2]. Furthermore, large ω_n increases the amplitude offset and the estimated frequency ripple, as presented in section 3.3. For the chosen parameters, the detection threshold is close to 1.4 pu. This value is smaller than the nondetection zone imposed by the SOGI bandwidth. Therefore, for the adjustment considered in this work, the SRF-PLL structure does not increase the nondetection zone of the harmonic detector.

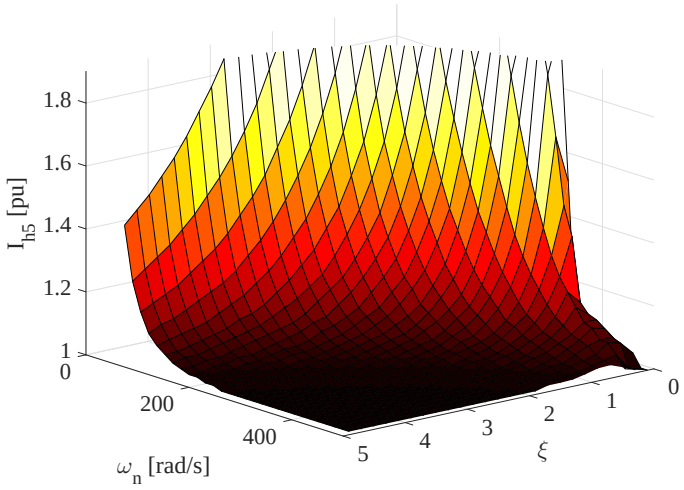

Figure 8: SRF-PLL detection threshold in function of ξ and ω_n considering a transition from 3rd to 5th harmonic order.

3.5. Control Stability Analysis

Considering the solar plant and the dc-link represented by a dc-bus voltage source and neglecting the load and the grid impedance, the grid-connected

photovoltaic system, as depicted in Fig. 1a, can be modelled as:

$$P_L(z) = \frac{\left(1 - e^{\frac{R_f T_s}{L_f}}\right) z^{-2}}{\left(1 - z^{-1} e^{\frac{R_f T_s}{L_f}}\right) R_f}, \tag{14}$$

where L_f and R_f are the inductance and equivalent series resistance of the L filter, respectively [31, 35].

The error rejection between the inverter current $i_s(z)$ and its reference $i_s^*(z)$ can be expressed as:

$$\frac{E(z)}{i_s^*(z)} = \frac{1}{1 + G_c(z) P_L(z)}, \tag{15}$$

where $E(z)$ is the error expressed as $i_s^*(z) - i_S(z)$. The function $1 + G_c(z)P_L(z)$ is known as the distance of the open loop transfer function $G_c(z)P_L(z)$ to the critical point $-1 + 0j$ at each frequency in the Nyquist diagram. For resonant controllers applied in simple system, the minimum distance η_h of $[K_p^r + K_{ih} R_x(z)]P_L(z)$ to the critical point is more reliable and compact indicator of system stability than analysis by means of margin and phase gains [31, 35].

Besides to reach an admissible η_h, the K_p^r gain is set to ensure that the crossover frequency f_c of $K_p^r P_L(z)$ is lower than a decade below the switching frequency to effectively filter the commutation harmonics.

It is considered the PR controller tuned at the 3rd harmonic frequency $R_3(z)$ to illustrate the K_p^r influence on the minimum distance to the critical point in the Nyquist diagram. Fig. 9a and Fig. 9b shows the Nyquist diagrams of $[K_p^r + K_{ih} R_3(z)]P_L(z)$ for two K_p^r values (15, 29). For very large values of K_i, the effect on stability can be neglected. Fig. 9c and Fig. 9d shows the closed loop poles displacement for the same K_p^r values with resonant frequency variation in $R_h(z)$, between $\omega_h = 2\pi 180\ rad/s$ and $\omega_h = 2\pi 1260\ rad/s$. The red colour poles indicates when its position is outside the unit circle in the z-plane.

For $K_p^r = 15$, the minimum distance is 0.81, as depicted in Fig. 9a. However, the system becomes unstable at the frequency $\omega_h = 2\pi 633\ rad/s$, as shown in

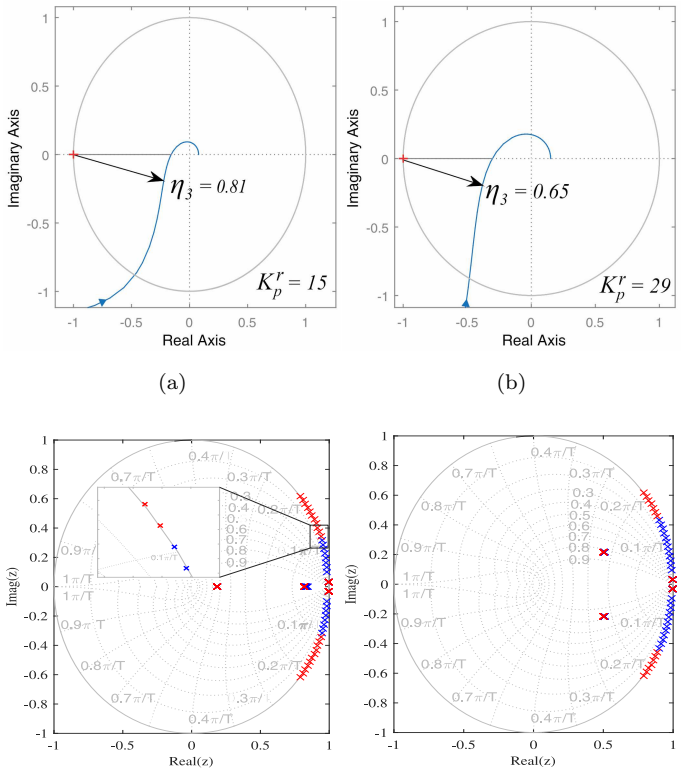

Figure 9: Nyquist diagrams of $[K_p^r + K_{ih} R_3(z)] P_L(z)$ and the closed loop poles displacement during resonant frequency variation in $R_h(z)$ between $\omega_h = 2\pi 180\ rad/s$ and $\omega_h = 2\pi 1260\ rad/s$ for two values of K_p^r (15 and 29). Parameters: $L_f = 8\ mH$, $R_f = 80\ m$, sampling period $T_s = 1/12000\ s$, $K_f = 1000$ and $K_i h = 5000$, (a) $K_p^r = 15$, (b) $K_p^r = 29$, (c) $K_p^r = 15$ and (d) $K_p^r = 29$.

Fig. 9c, and thus the PMR controller presents a narrow frequency margin which can act. For $K_p^r = 29$ the minimum distance is 0.65, as illustrated in Fig. 9b, and the system becomes unstable at the frequency $\omega_h = 2\pi 903\ rad/s$ (Fig. 9d). However, the control is stable if tuned until 15th harmonic order, which are the common harmonics currents in the power system.

Moreover, in this case, the crossover frequency ($f_c = 580\ Hz$) is lower than a decade below the switching frequency, attending the minimal design specifi-

cations. For large values of K_p^r, the PMR controller presents an wide frequency margin of action. However, the minimum distance to the critical point is reduced. Moreover, the crossover frequency of the $K_p^r P_L(z)$ becomes closer to the switching frequency ($f_s = 6000\ Hz$) with the increase of $K_p^r P_L(z)$.

In order to achieve the minimum distance to the critical point and to ensure the crossover frequency lower than a decade below the switching frequency, for this work $K_P^r = 29$ is chosen.

4. Results

4.1. Simulation Results

The case study presents a solar array with 4 parallel strings of 15 panels of 48 W in series connection. The simulation was implemented in Matlab/Simulink environment with simulation time of 4.5 seconds. Parameters of the simulation system are presented in Table 1.

Table 1: Parameters of the simulation setup.

System Parameters	**Value**
Switching frequency	6 kHz
Sampling frequency	12 kHz
Filter parameters	8 mH/80 $m\Omega$
Dc-bus voltage	390 V
PCC parameters	220 V/60 Hz
Solar Irradiance	600 W/m^2
Injected Power	1.55 kW
Current control parameter	**Value**
Resonant controller gains	$K_p^r = 29$, $K_{if} = 1000$ and $K_{ih} = 5000$
Fundamental SRF-PLL gains	$k_{p,pll,f} = 26.66$ and $k_{i,pll,f} = 355.31$
Harmonic SRF-PLL gains	$k_{p,pll,h} = 444.3$ and $k_{i,pll,h} = 98696.04$
filter f_{cf} cut-off frequency	10 Hz
filter f_{ca} cut-off frequency	5 Hz
SOGI gain	1.4142

In this simulation, the load harmonic current contents are changed to validate the proposed harmonic detection method and the adaptive control strategy. The nonlinear loads connected to the PCC are represented by current sources, emulating the harmonic characteristics of the load current. The load current spectrum during the simulation time intervals are shown in Fig. 10.

Fig. 11a and Fig. 11b shows the amplitude and frequency detection of the predominant harmonic in the load current. The harmonic detection is enabled at 0.5 seconds. Between $0.5 < t < 1.5$ seconds, the 3rd harmonic component with amplitude equal to 3 A is detected. Between $1.5 < t < 3$ seconds, the 7th harmonic component with amplitude equal to 2 A is detected. Between $3 < t < 4.5$ seconds, the 5th harmonic component with amplitude equal to 4 A is predominant in the load harmonic current and it is detected.

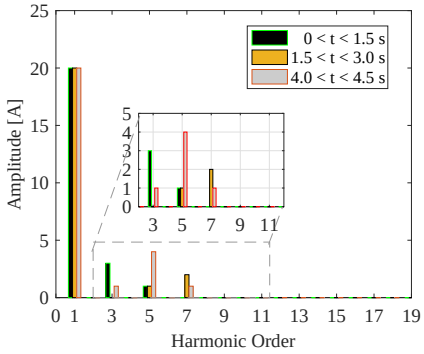

Figure 10: Load current spectrum.

After the load current harmonic detection, the resonant controller is automatically tuned in the detected frequency and load harmonics are compensated by the inverters. Using the proposed control strategy, the inverter compensates the 3rd harmonic content of the load current, which is eliminated from the grid current, as depicted in Fig. 12a. Furthermore, the inverter injects 10 A of active current into the grid (1.55 kW). Fig. 12b shows the inverter injecting 7th harmonic content to eliminate it from the grid current. It can be seen that the 7th harmonic of the grid current is strongly reduced. In the last analysis, the 5th

harmonic is predominant in amplitude, as depicted in Fig. 12c. In this case, the inverter compensates the 5th harmonic content of the load, and this component is strongly reduced in grid current. Fig. 13a and Fig. 13b shows the inverter current (i_S) and its reference (i_S^*) during harmonic detection transients. It can be seen that the control remains stable even in the detection transitions.

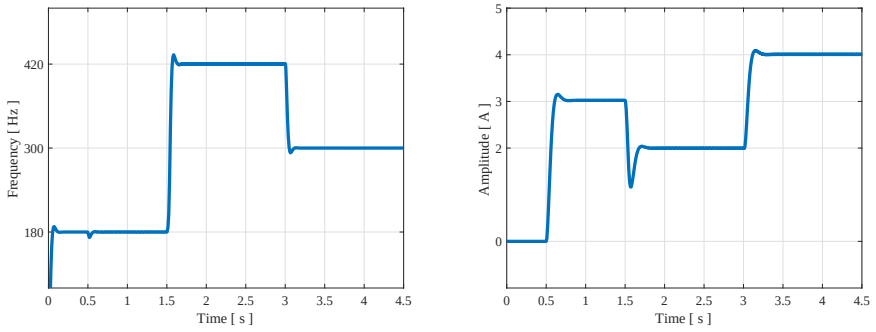

(a) (b)

Figure 11: Detected harmonic component of the load current. The system became operational at 0.5 seconds,(a) Detected frequency of the predominant harmonic in the load current and (b) Detected amplitude of the predominant harmonic in the load current.

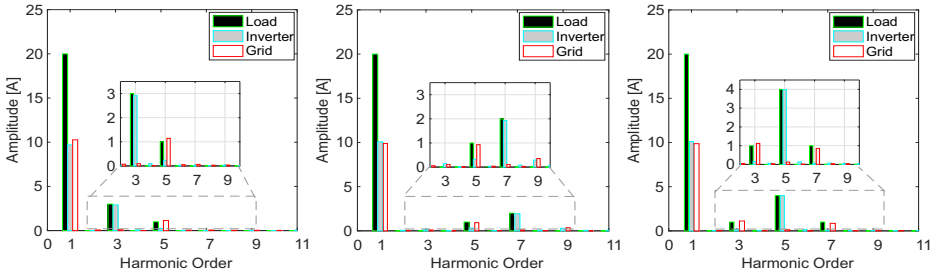

(a) (b) (c)

Figure 12: Current spectra during harmonic compensation between $0 < t < 4.5$ seconds, (a) $0 < t < 1.5$ seconds, (b) $1.5 < t < 3.0$ seconds and (c) $3.0 < t < 4.5$ seconds.

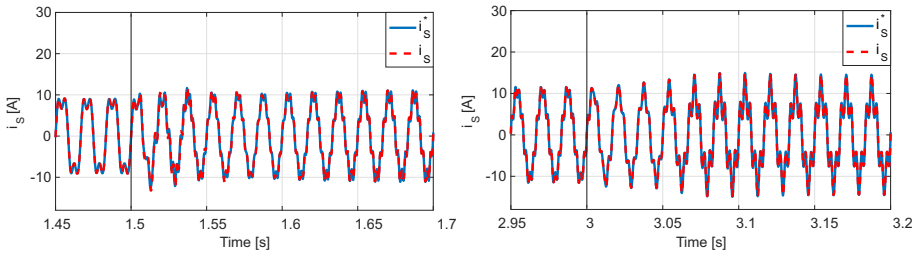

(a) (b)

Figure 13: Inverter current (i_s) and its reference (i_S^*) during the detection transients , (a) Transient at 1.5 seconds , (b) Transient at 3 seconds .

4.2. Experimental Results

Similar tests are also conducted in a laboratory prototype whose parameters are presented in Table 2. A single-phase power inverter is connected to different loads with characteristics presented in Table 3, in order to test the performance of the harmonic detector and compensation algorithms. The control algorithm was implemented in a Texas Instruments floating point DSP F28335.

Table 2: Parameters of the experimental setup.

System Parameters	**Value**
Switching frequency	6 kHz
Sampling frequency	12 kHz
Filter parameters	8 $mH/80$ $m\Omega$
Dc-bus voltage	60 V
PCC parameters	45 $V/60$ Hz
Current control parameter	**Value**
Resonant controller gains	$K_p^r = 5.9$, $K_{if} = 1000$ and $K_{ih} = 5000$
Fundamental SRF-PLL gains	$k_{p,pll,f} = 26.66$ and $k_{i,pll,f} = 355.31$
Harmonic SRF-PLL gains	$k_{p,pll,h} = 444.3$ and $k_{i,pll,h} = 98696.04$
filter f_{cf} cut-off frequency	10 Hz
filter f_{ca} cut-off frequency	5 Hz
SOGI gain	1.4142

Table 3: Characteristics of loads used in the experimental setup.

Load type	**Harmonic Content**
Load 1	3, 5, 7, 9...
Load 2	5, 7, 11...
Load 3 = Load 1 + Load 2	3, 5, 7, 9...
Harmonic Spectrum	**Predominant harmonic order**
Fig. 14b	3rd order — 180 Hz
Fig. 14c	5th order — 300 Hz
Fig. 14d	5th order — 300 Hz

The system operation starts with load 1 connected to the grid. At $t = 0.5$ seconds this load is disconnected and load 2 is connected at $t = 0.6$ seconds. Finally, at $t = 1.8$ seconds load 1 is turned on again and both loads 1 and 2 remains connected to the grid.

The dynamic behaviour of the detected amplitude and frequency are presented in Fig. 14a. The harmonic detection algorithm follows the harmonic component with higher amplitude of the load current. When load 1is disconnected, the detected amplitude stabilizes close to zero. After, load 2 is connected and the frequency increases from 180 Hz to 300 Hz. When both loads are connected, the higher harmonic component is kept in the 5th harmonic order. Therefore, only the detected amplitude changes.

Current waveforms and PCC voltage in steady state are shown in Fig. 15a shows the waveforms before the compensation. As can be observed, the grid current is distorted due to load current harmonic content, and the inverter active current reference remains in 3 A during all tests.

Fig. 15b shows the current waveforms for load 1. Current harmonic spectra for this situation is presented in Fig. 14b. Using the proposed control strategy, the inverter compensates the third harmonic content of the load. This harmonic is almost eliminated from the grid current, as depicted in Fig. 14b. Furthermore, the inverter continues to inject 3 A of fundamental active current into the grid. Fig. 15c shows the waveforms for load 2. Current harmonic spectra for this

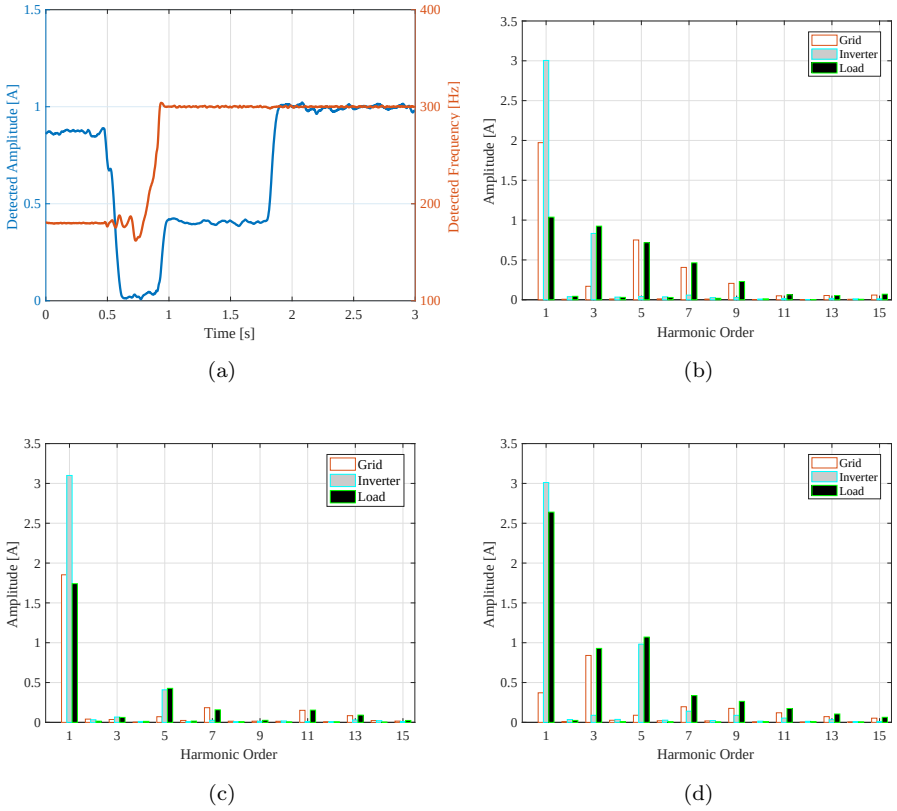

Figure 14: Experimental evaluation of the proposed current harmonic detector during load changes and harmonic spectra of the load, inverter and grid current for load 1, 2 and 3, (a) Detected amplitude and detected frequency of the load current, (b) Current harmonic spectra for load 1, (c) Current harmonic spectra for load 2 and (d) Current harmonic spectra for load 3.

test is presented in Fig. 14c. The harmonic detector follow the higher harmonic component and changes the detected frequency. By means of the adaptive resonant control, the inverter compensates the 5th harmonic content of the load, as shown in Fig. 14c. It can be seen that the 5th harmonic frequency is strongly reduced in the grid current.

Finally, Fig. 15d shows the waveforms for load 3 and the current harmonic spectrum for this situation is presented in Fig. 14d. The harmonic detector

follows the harmonic amplitude variation and the inverter compensates the 5th harmonic content of the load current. This component is strongly reduced in grid current.

385 The simulation and experimental results have shown the strongly reduction of the predominant harmonic component of the load current in the power system. The PMR controller has remained stable even during in its dynamic tuning through the proposed detection method.

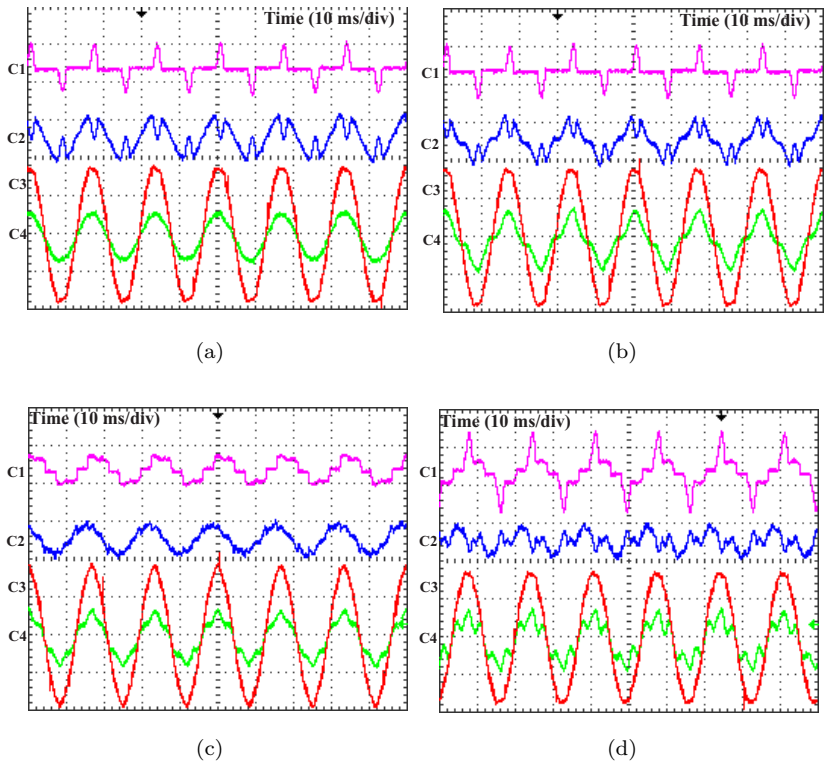

Figure 15: Voltage and currents waveforms in experimental setup during load changes: C1 Load Current (5 A/div); C2 Grid Current (5 A/div); C3 PCC Voltage (25 V/div) C4 Inverter Current (5 A/div), (a) System operating without harmonic compensation, (b) Compensation of the load 1 higher harmonic component, (c) Compensation of the load 2 higher harmonic component and (d) Compensation of the load 3 higher harmonic component.

5. Conclusion

An adaptive current harmonic control strategy applied in multifunctional single-phase photovoltaic inverters has been developed in this paper. This control strategy is based on the harmonic current detection method, which is designed to extract the load harmonic current with higher amplitude and its frequency. Thereby, the proportional multiple resonant current controller can be automatically tuned for specific harmonics, increasing efficiency and reducing the control algorithm complexity.

Analysis of the current harmonic detector and the effect of the algorithm parameters have been addressed. When the current harmonic content has harmonic orders with similar amplitude, a nondetection zone was described as well as the minimum condition to detect the harmonic content with higher amplitude during load current changes. Furthermore, control stability analysis of adaptive resonant controllers during frequency variations was presented.

Simulation and experimental results showed the proposed control strategy performance and the improvements in the grid current. The grid current THD is reduced by compensating the harmonic current of the nonlinear load connected to the PCC, using the photovoltaic converter.

In this way, if several photovoltaic systems are already installed into the power system, the modifications in the control strategy for partial harmonic compensation can result in considerable reduction of the grid current THD.

It is worth mentioning that the current harmonic detector proposed in this work can be used to detect more than one harmonic component. for this purpose, just add more stages of the SOGI-PLL structure in series connections.

6. Acknowledgments

The authors would like to thank CNPq (Conselho Nacional de Desenvolvimento Científico e Tecnológico), FAPEMIG (Fundação de Amparo á Pesquisa do estado de Minas Gerais) and CAPES (Coordenação de Aperfeiçoamento de Pessoal de Nível Superior) for their assistance and financial support.

References

[1] REN21, Renewables 2015 global status report, Tech. rep., REN21 Secretariat, Paris (2015).

[2] R. Teodorescu, M. Liserre, P. Rodrguez, Grid Converters for Photovoltaic and Wind Power Systems, Wiley-IEEE Press, 2011.

[3] F. Blaabjerg, Z. Chen, S. Kjaer, Power electronics as efficient interface in dispersed power generation systems, IEEE Trans. Power Electron. 19 (5) (2004) 1184–1194.

[4] Y. Yang, F. Blaabjerg, H. Wang, Low-voltage ride-through of single-phase transformerless photovoltaic inverters, IEEE Trans. Ind. Appl. 50 (3) (2014) 1942–1952.

[5] Y. Yang, H. Wang, F. Blaabjerg, Reactive power injection strategies for single-phase photovoltaic systems considering grid requirements, IEEE Trans. Ind. Appl. 50 (6) (2014) 4065–4076.

[6] N. Espinoza, M. Bongiorno, O. Carlson, Novel LVRT testing method for wind turbines using flexible VSC technology, IEEE Trans. Sustain. Energy 6 (3) (2015) 1140–1149.

[7] V. Miñambres-Marcos, M. Á. Guerrero-Martínez, E. Romero-Cadaval, P. González-Castrillo, Grid-connected photovoltaic power plants for helping node voltage regulation, IET Renew. Power Gener. 9 (3) (2015) 236–244.

[8] J. P. Bonaldo, H. K. M. Paredes, J. A. Pomilio, Control of single-phase power converters connected to low voltage distorted power systems with variable compensation objectives, IEEE Transactions on Power Electronics 31 (3) (2016) 2039–2052.

[9] L. S. Xavier, A. F. Cupertino, H. A. Pereira, Adaptive saturation scheme for a multifunctional single-phase photovoltaic inverter, in: IEEE/IAS International Conference on Industry Applications, 2014, pp. 1–8.

[10] L. S. Xavier, J. H. de Oliveira, A. F. Cupertino, V. F. Mendes, H. A. Pereira, Saturation scheme for single-phase photovoltaic inverters in multi-functional operation, in: IEEE 24th International Symposium on Industrial Electronics, 2015, pp. 1392–1397.

[11] G. Tsengenes, G. Adamidis, Investigation of the behavior of a three phase grid-connected photovoltaic system to control active and reactive power, Electric Power Systems Research 81 (1) (2011) 177 – 184.

[12] C. Chen, J. Wu, I. Yen, C. Moo, Harmonic analysis of distribution systems, Electric Power Systems Research 17 (3) (1989) 171 – 177.

[13] J. Arrillaga, N. R. Watson, Power System Harmonics, 2nd Edition, Hoboken, NJ, USA: Wiley, 2003, 2003.

[14] F. C. De La Rosa, Harmonics and Power Systems, CRC Press, 2006.

[15] L. Sainz, J. J. Mesas, A. Ferrer, Characterization of non-linear load behavior, Electric Power Systems Research 78 (10) (2008) 1773 – 1783.

[16] IEEE recommended practices and requirements for harmonic control in electrical power systems, IEEE Std 519-1992 (1993) 1–112.

[17] Assessment of emission limits for distorting loads in MV and HV power systems, IEC Standard 61000-3-6 (1).

[18] H. Paredes, D. Brandao, T. Terrazas, F. Marafao, Shunt active compensation based on the conservative power theory current's decomposition, in: XI Brazilian Power Electronics Conference (COBEP), 2011, pp. 788–794.

[19] H. Akagi, Y. Kanazawa, A. Nabae, Instantaneous reactive power compensators comprising switching devices without energy storage components, IEEE Trans. Ind. Appl. IA-20 (3) (1984) 625–630.

[20] E. H. Watanabe, H. Akagi, M. Aredes, Instantaneous p-q power theory for compensating nonsinusoidal systems, in: International School on Nonsinusoidal Currents and Compensation, 2008.

[21] R. S. Herrera, P. Salmeron, Present point of view about the instantaneous reactive power theory, IET Power Electronics 2 (5) (2009) 484–495.

[22] N. R. Tummuru, M. K. Mishra, S. Srinivas, Multifunctional VSC controlled microgrid using instantaneous symmetrical components theory, IEEE Trans. Sustain. Energy 5 (1) (2014) 313–322.

[23] Y. F. Wang, Y. W. Li, Three-phase cascaded delayed signal cancellation PLL for fast selective harmonic detection, IEEE Trans. Ind. Electron. 60 (4) (2013) 1452–1463.

[24] A. F. Cupertino, L. P. Carlette, F. Perez, J. T. Resende, S. I. Seleme, H. A. Pereira, Use of control based on passivity to mitigate the harmonic distortion level of inverters, in: IEEE PES Conference On Innovative Smart Grid Technologies Latin America, 2013.

[25] J. He, Y. W. Li, F. Blaabjerg, X. Wang, Active harmonic filtering using current-controlled, grid-connected DG units with closed-loop power control, IEEE Trans. Power Electron. 29 (2) (2014) 642–653.

[26] M. Ciobotaru, R. Teodorescu, F. Blaabjerg, A new single-phase PLL structure based on second order generalized integrator, in: IEEE Power Electronics Specialists Conference, 2006.

[27] Y. Yang, K. Zhou, F. Blaabjerg, Frequency adaptability of harmonics controllers for grid-interfaced converters, International Journal of Control (2015) 1–12.

[28] X. Guillaud, P. Degobert, R. Teodorescu, Use of resonant controller for grid-connected converters in case of large frequency fluctuations, in: European Conference on Power Electronics and Applications, 2007.

[29] D. Sera, T. Kerekes, R. Teodorescu, F. Blaabjerg, Improved MPPT method for rapidly changing environmental conditions, in: IEEE International Symposium on Industrial Electronics, Vol. 2, 2006.

[30] M. G. Villalva, J. R. Gazoli, E. R. Filho, Comprehensive approach to modeling and simulation of photovoltaic arrays, IEEE Trans. Power Electron. 24 (5) (2009) 1198–1208.

[31] A. G. Yepes, Digital resonant current controllers for voltage source converters, Ph.D. thesis, University of Vigo (2011).

[32] S. Golestan, J. M. Guerrero, Conventional synchronous reference frame phase-locked loop is an adaptive complex filter, IEEE Trans. Ind. Electron. 62 (3) (2015) 1679–1682.

[33] R. E. Best, Phase-Locked Loops: Design, Simulation, and Applications, 5th Edition, New York: McGraw-Hill Professional, 2003.

[34] F. M. Gardner, Phaselock Techniques, 3rd Edition, John Wiley & Sons, Hoboken, NJ, USA, 2005.

[35] A. Yepes, F. Freijedo, O. Lopez, J. Doval-Gandoy, Analysis and design of resonant current controllers for voltage-source converters by means of nyquist diagrams and sensitivity function, IEEE Transactions on Industrial Electronics 58 (11) (2011) 5231–5250.